Energy Conversion and Management: X 30 (2026) 101685

Contents lists available at ScienceDirect

Energy Conversion and Management: X

journal homepage: www.sciencedirect.com/journal/energy-conversion-and-management-x

A holistic framework for optimal ship energy system design, including operational requirements, lifetime cost, and vessel stability

Foivos Mylonopoulos *, Andrea Coraddu, Henk Polinder

Department of Maritime and Transport Technology, Delft University of Technology, Delft 2628 CD, the Netherlands

ARTICLE INFO

Keywords:
Hydrogen
Ship energy systems
System design
Lifetime cost
Ship stability
Optimization

ABSTRACT

Low total lifetime cost is essential for the adoption of zero-emission ship energy systems, which must meet operational power demands while complying with onboard safety regulations. However, many studies rely on a simplified, averaged or insufficiently representative load profile and treat system design, operation, and integration feasibility separately, which can distort lifetime cost assessments and result in practically infeasible retrofit concepts. This study investigates how a hydrogen-based ship energy system can be optimally sized, operated, and arranged onboard to minimize total lifetime cost while satisfying operational constraints and stability requirements for a general cargo vessel retrofit. A representative power profile is synthesized from one year of operational data using a probability-based downsampling method and then used in a mixed-integer nonlinear lifetime cost optimization with discrete placement and ballast decisions, solved using the SCIP solver. The optimal retrofit comprises 1.4 MW of fuel cells, 180 kWh of batteries, and a 146 m^3 liquefied hydrogen (LH_2) tank, requires 171 t of ballast to satisfy trim and vertical stability constraints, and is primarily driven by fuel costs, which account for 74% of the total lifetime cost. Overall, the results indicate that the viability of hydrogen-based ship retrofits primarily depends on LH_2 storage integration constraints and hydrogen price assumptions, and that the proposed framework provides a practical basis for lifetime cost assessment of feasible retrofit designs.

1. Introduction

1.1. Background

The International Maritime Organization (IMO) has imposed stringent regulations to reduce shipping emissions [1]. In the short term, carbon emissions must be reduced by 40% by 2030 and by at least 70% by 2040, relative to 2008 levels [2]. The adoption of green fuels and novel energy systems for both newbuilds and retrofits is a key driver in achieving the maritime emission targets. Hydrogen fuel cells and lithium-ion batteries are promising zero-emission alternatives to drive the maritime energy transition, especially for short-sea operations near refuelling and recharging infrastructure [3,4].

The applicability of hydrogen-based ship systems remains limited due to the low technical maturity, limited availability of cheap green hydrogen, high investment costs, and insufficient infrastructure. This study aims to accelerate the maritime energy transition by providing insights into the optimal design and operation of ship energy systems integrating hydrogen fuel cells and batteries. The focus is on retrofitting existing vessels and optimizing system topology and operation from a holistic perspective considering operational needs, lifetime cost and ship stability.

1.2. Literature review

A comprehensive review of methods for the design and control of energy systems is provided in [5], emphasizing the importance of integrating design and operational considerations in optimization problems.

Several studies reduce computational complexity by adopting linear or mixed-integer linear formulations and using simplified or averaged power profiles. Bassam et al. [6] conducted a system sizing optimization for a passenger ferry, evaluating various fuel cell-battery combinations to minimize the total energy system cost. Power distribution was managed using a Proportional-Integral controller, without optimizing the operational parameters. The analysis was based on a single profile with an extended period of nearly constant power output, rather than a representative sailing cycle derived from the operational data. Pivetta et al. [7] applied a Mixed Integer Linear Programming (MILP) algorithm

* Corresponding author.
E-mail address: F.P.Mylonopoulos@tudelft.nl (F. Mylonopoulos).

https://doi.org/10.1016/j.ecmx.2026.101685
Received 21 November 2025; Received in revised form 13 February 2026; Accepted 14 February 2026
Available online 16 February 2026

to optimize daily costs and fuel cell degradation for three passenger vessels of different sizes, with battery degradation incorporated as a constraint. Dall'armi et al. [8] used the same algorithm, for an optimal design and operation study, aiming to minimize the fuel consumption and degradation of both fuel cells and batteries in one of the three passenger vessels, with a focus on the progressive aging of the power supply systems. In [7] and [8], the system weight and volume were set as optimization constraints, considering that the combined system weight and volume of the retrofitted components (fuel cells, batteries, tank) would be lower than those of the original diesel engine. The same authors extended their work in [9], by incorporating uncertainties related to fuel and component costs, without considering the impact of different power profiles on the results. As noted in [6,8], the hydrogen consumption had the most significant influence on the optimal solution. In [7–9], a hierarchical objective approach was used, with linear objective functions to simplify the optimization process. Similarly in [10], a non-convex bi-objective optimal control problem was transformed into a convex framework to facilitate computation using MOSEK optimization software.

Many studies optimize control/energy management parameters for fixed system designs. Zhang et al. [11] applied a real-time equivalent consumption minimization strategy to enhance the system efficiency and reduce the fuel cell and battery degradation. Supercapacitors were integrated to handle high transient loads. The fuel cells were sized to meet the average load demand, while the power distribution between the supercapacitors and the batteries was managed using a high-pass filter. Several other studies [12–14] have also optimized energy management strategies for fuel cell-battery hybrid powertrains with fixed design parameters. In [15,16], supercapacitors were integrated into hybrid energy storage systems to improve system efficiency and reduce battery degradation using fuzzy logic controllers. Fan et al. [17] proposed a control strategy for optimal power coordination, leveraging pre-voyage and intra-voyage information to minimize the costs and emissions. This optimization problem was solved in two stages using the column and constraint generation algorithm.

A few studies have presented combined energy system design and control optimization, but without considering the impact of system placement onboard and the effects of different system arrangements on ship stability. Vieira et al. [18] optimized the system configuration and operation of a hybrid platform supply vessel to minimize carbon emissions by varying the sizes of the components. Wang et al. [19] conducted a nested design and control optimization for a fixed number of diesel gensets, fuel cells and batteries, allowing for variable rated capacities. A MILP algorithm was used in the inner layer for the operation optimization and a genetic algorithm in the outer layer for the design optimization. Various system topologies were analyzed based on low, medium, and high emission reduction targets. Similarly, Wu and Bucknall [20] implemented a two-layer optimization using deterministic dynamic programming. Their study focused on lifetime emission reduction after retrofitting a diesel-mechanical coastal ferry with hydrogen fuel cells and batteries. The analysis was based on a simplified averaged power profile. Si et al. [21] combined fuzzy logic rules with the artificial bee colony algorithm to optimize the design and operation of a bulk carrier integrating photovoltaic panels, fuel cells, batteries, wind turbines, and diesel generators. This study did not provide a detailed discussion of the practical challenges associated with weight, volume, integration, safety, and reliability when including multiple energy systems into a single design. Chen et al. [22] proposed a sizing and energy management optimization framework for a hydrogen-fuelled vessel with a hybrid energy storage system using a support vector machine and frequency control. The weighted sum method prioritized energy efficiency, followed by battery degradation, with bus voltage fluctuations assigned the lowest importance. This study did not explore different pareto front solutions across a wide range of weighting coefficients. Ganjian et al. [23] conducted an optimal design study for a fishing boat powered by hydrogen fuel cells and batteries. As claimed, this was the first study to use volume as an objective function. The interactions between different objectives (electrical safety, cost, and volume) were not considered, as each was solved independently using single-objective formulations.

1.3. Literature gaps

The key findings and gaps identified in the literature review are summarized below:

- Few studies have explored the combined optimization of system topology and operation for ship energy systems, particularly from a holistic perspective. Most research focuses on optimizing energy management strategies for a predetermined (fixed) design.
- Ship stability and system placement constraints are often overlooked and not integrated into energy system optimization models, which may lead to infeasible design solutions. In ship retrofits, trim and vertical stability constraints are particularly critical.
- To reduce computational complexity, ship energy system optimization problems are frequently simplified into linear, quadratic, or mixed-integer linear formulations. However, these relaxations and simplifications may lead to suboptimal solutions.
- Many studies rely on simplified, smoothed, averaged, arbitrarily selected or insufficiently representative power profiles for optimization, which may distort lifetime cost assessments.
- Few studies optimize energy system total lifetime cost, despite this being a crucial factor for shipowners' decision-making.

1.4. Research focus and key contributions

The focus of this research is on the optimal energy system topology and operation of a general cargo vessel from a holistic perspective. The original diesel mechanical propulsion system of the ship is conceptually replaced by a hydrogen-hybrid powertrain to reduce emissions. A probability-based downsampling approach is used to generate a representative power profile in terms of fuel consumption and fuel cell degradation, based on the annual propulsion data. The power and propulsion systems are optimized to minimize the total lifetime cost including fuel, capital and system replacement costs, while ensuring compliance with the safety and ship stability constraints. The optimization is a Mixed Integer, Nonlinear Programming (MINLP) problem incorporating binary decision variables and combinatorial aspects, and is solved using a specialized MIP solver. Overall, this study provides a holistic framework for the optimal design and operation of ships with novel energy systems, aligning operational needs, lifetime cost efficiency, and regulatory requirements.

The key contributions of this study are summarized below:

- Development of a holistic framework for the optimal topology and operation of ship energy systems, minimizing total lifetime costs while considering operational requirements and vessel stability regulations.
- Formulation of a global optimization framework to solve complex MINLP problems for ship energy systems, utilizing a specialized MIP solver to efficiently handle computational complexity and ensure high-quality solutions.
- Development and implementation of a probability-based downsampling method to generate a representative power profile from annual measurements, enabling computationally-efficient lifetime cost optimization while preserving fuel consumption and fuel cell degradation estimates within an acceptable threshold.

The remainder of this paper is structured as follows: Section 2 introduces the case vessel and its powerplant components. Section 3 presents the methodology for optimal system topology and operation, incorporating stability constraints. Section 4 presents and discusses the

optimization results. Finally, Section 5 provides concluding remarks and recommendations for future research directions.

2. Case study

The case vessel is a short-sea general cargo ship operating primarily in the Baltic and North Sea, without a fixed route or schedule. Its length is 90 m and its breadth is 12.5 m [24,25]. The original diesel-powered configuration has a mechanical propulsion system with a single oversized 1800 kW main engine and a controllable pitch propeller (direct-drive system without gearbox). In this study, the vessel is conceptually retrofitted with proton exchange membrane fuel cells and lithium iron phosphate batteries to reduce its environmental footprint. Fuel cells and batteries generate electricity which is supplied to the direct current (DC) bus via DC/DC converters. Excess fuel cell power can be used to charge the batteries onboard. After the DC distribution system, the electric current is converted to alternating current (AC) through inverters, delivering power to the propulsion motors that drive the ship's propeller, through a reduction gearbox. The focus of this study is to determine the optimal total capacities of fuel cells and batteries, and the optimal power distribution between these sources, to minimize the total lifetime cost, while ensuring compliance with regulatory requirements for equipment placement and ship stability.

3. Methodology

Fig. 1 presents a flowchart illustrating the proposed methodology for this study.

The methodology is divided into two main steps:

- Step 1: The onboard measured power demand data of the ship's load profiles are analyzed, and a representative power profile is generated.
- Step 2: The combined optimal system topology and operation problem is formulated and solved, using the representative profile from Step 1 as input. The total system lifetime cost is optimized, and the optimal design, including ship stability constraints, is obtained using Python interfaced with the specialized MIP solver SCIP.

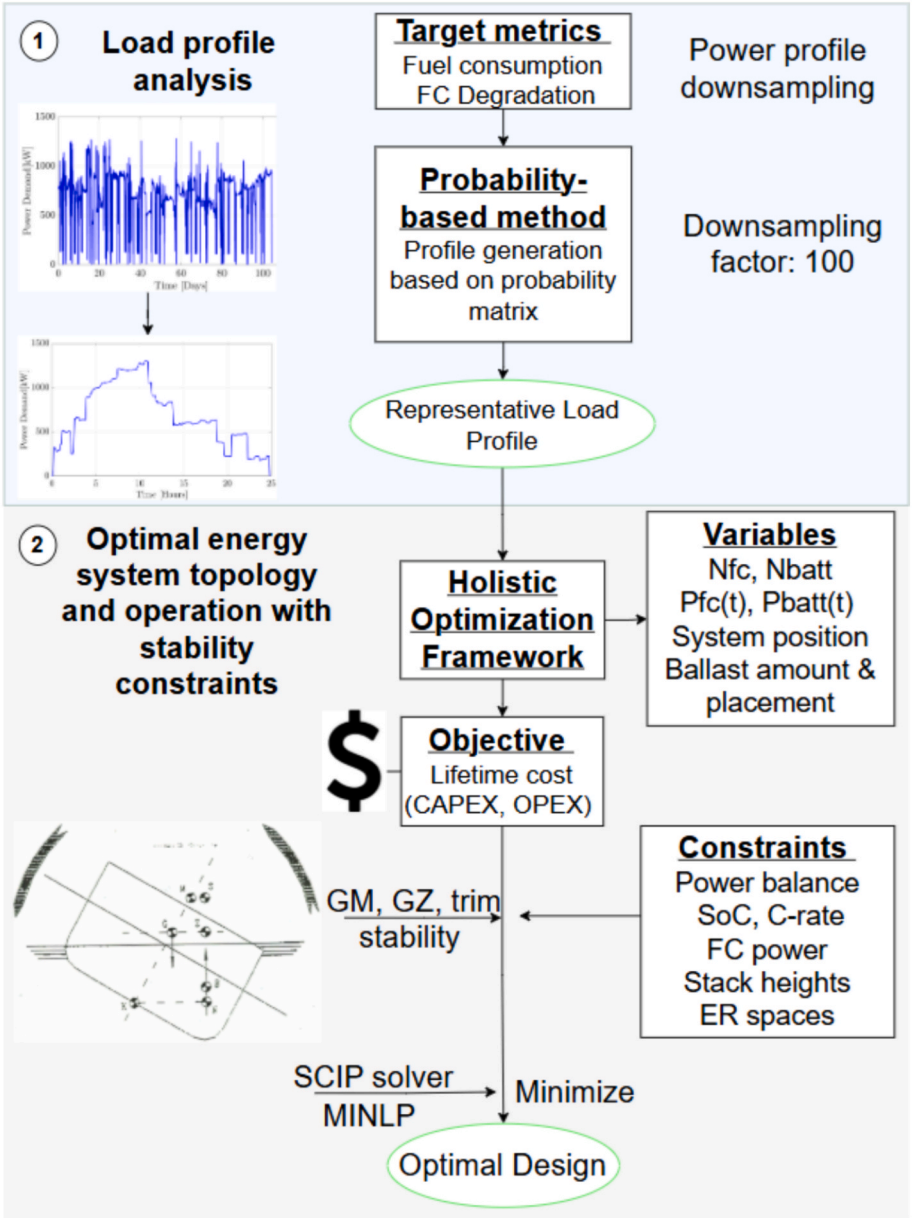

Fig. 1. Methodology for power profile analysis and optimization.

3.1. Ship power profile analysis and synthesis

Fig. 2 presents the propulsion power profile derived from the measured diesel-engine power output of the vessel in its original configuration. The data were collected by the vessel operator from on-board monitoring sensors over a one-year period (2022). The dataset includes multiple trips, routes and operating conditions, and represents the vessel's complete annual sailing activity excluding port stays. The annual profile (Fig. 2) spans approximately 100 sailing days and is assumed to be repeated twice every year over the vessel's lifetime.

Since the case ship operates across multiple routes and under varying operating conditions, directly optimizing over the full annual power profile (30,000 data at a 5-minute resolution) is computationally intensive. Therefore, a representative profile is generated from the full annual dataset to enable accurate and computationally-efficient design and operation analysis.

One-year of diesel engine power data, recorded at a 5-minute sampling interval (Fig. 2), are analyzed using a probability-based approach to generate a representative timeseries. A downsampling factor of 100 is applied, reducing the original 30,000 operational data (corresponding to 100 sailing days excluding port stays) to a reduced dataset of 300 data (1 sailing day) that can be efficiently handled by the available computational power. The representativeness of the reduced power profile is assessed by comparing fuel consumption and fuel cell degradation estimates obtained from the reduced dataset against those calculated using the full annual dataset. Deviations of up to ± 5% in fuel consumption and fuel cell degradation between the reduced profile (300 data) and the full annual dataset (30,000 data) are considered acceptable, and the reduced representative profile can be used for the lifetime cost optimization. The ± 5% tolerance reflects realistic operational variability (e.g., weather, trim changes, navigation decisions) and represents a small margin given the substantial reduction in dataset size.

Fuel consumption is calculated using Eq. (1):

$$F_{FC}(t) = a \bullet P_{FC}^2(t) + b \bullet P_{FC}(t) + c \tag{1}$$

where $F_{FC}(t)$ and $P_{FC}(t)$ are the fuel consumption and power output of the fuel cell as functions of time, respectively. The coefficients a, b, and c are 0.0066, 1.4025, and 1.8306 respectively, derived from the efficiency curve of a 100 kW stack as provided by the manufacturer [26].

The total fuel consumption of a single voyage (F_{total}) is computed in kilograms (kg) using Eq. (2):

$$F_{total} = N_{FC} \sum_{t=0}^{t_{final}} (F_{FC}(t) \bullet \Delta t \bullet k_{e\to m}) \tag{2}$$

where:

- t represents discrete time steps over the power profile duration
- $\Delta t = 0.0833$ h (5 min) is the sampling interval.

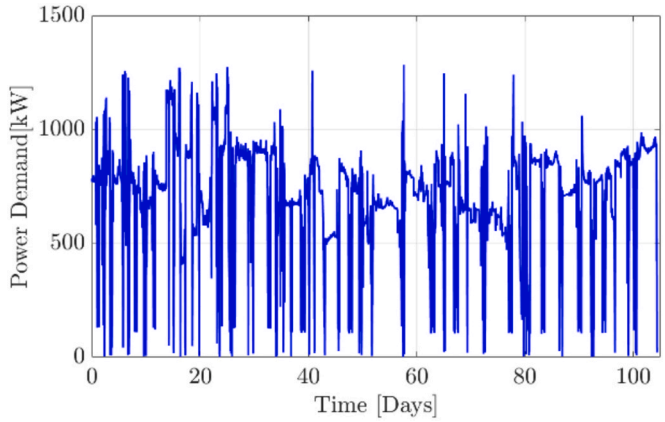

Fig. 2. Diesel engine annual power data.

- $k_{e\to m} = 0.03$ kg/kWh is the energy-to-mass conversion coefficient [27].

Based on [25], fuel cell degradation is dominated by transient loading effects. Therefore, a transient load-based degradation-proxy (D_{FC}) is computed as the cumulative absolute change in fuel cell power between successive time steps (Eq. (3)) and is used only for relative comparison of load ramping behaviour between the reduced and the full annual profile.

$$D_{FC} = \sum_{t=1}^{t_{final}} |P_{FC}(t) - P_{FC}(t-1)| \tag{3}$$

3.1.1. Probability-based profile generation method

The representative load profile is generated using a probability-based approach in which a probability matrix is constructed from the full annual dataset. The original dataset, consisting of 30,000 data, is structured into a matrix, where:

- Rows correspond to power changes between successive 5-minute intervals.
- Columns represent power value intervals (e.g., 0–100, 100-200… 1200-1300 kW).

Each matrix entry represents the number of data that fall within a specific combination of power range and power-change category. To generate a reduced dataset, the matrix is normalized to represent the probability of occurrence of each power-level and power-change combination. For example, in the original annual dataset containing 1,000 data within the 600–700 kW power range and 0–1 kW power-change category, a reduced dataset of 300 points (corresponding to a downsampling factor of 100) should contain approximately 10 such data to preserve representativeness.

The reduced power profile is generated by random sampling from the joint probability distribution defined by the matrix. The resulting profile is then evaluated by comparing fuel consumption and fuel cell degradation estimates obtained from the reduced dataset against those calculated using the full annual profile. Deviations within predefined tolerance limits (±5%) are considered acceptable. Lower downsampling factors increase the likelihood of obtaining a representative profile within fewer iterations, but they also increase the number of data and, consequently, the computational time required for simulations.

An alternative algorithmic downsampling approach based on the Ramer Douglas Peucker (RDP) algorithm [28] was also evaluated. However, the probability-based approach is used for all analyses presented in this work. Details of the RDP-based approach are provided in Appendix A.

3.2. Optimal system topology and operation

In this section, the framework for the simultaneous design and operation optimization problem including system operation, placement and ship stability constraints is presented.

3.2.1. System operation constraints

The main energy systems required for the retrofitted hydrogen-based version include fuel cells, hydrogen tank, batteries, converters, DC switchboard, inverter, propulsion motor, and gearbox.

The operational constraints of the fuel cell system are shown in Eqs. (4)–(6):

$$P_{FC,min} \le P_{FC}(t) \le P_{FC,max} \tag{4}$$

$$|P_{FC}(t) - P_{FC}(t+1)| \le P_{FC,max} - P_{FC,min} \tag{5}$$

$$P_{FC,initial} = P_{FC,final} = P_{FC,min} \tag{6}$$

The fuel cell power is constrained within 10–100% of its rated

capacity, as expressed in Eq. (4) [26]. Eq. (5) defines the ramping constraint, assuming that the fuel cell can increase or decrease power across its entire operational range within successive 5-minute intervals [26]. Finally, Eq. (6) imposes a boundary condition, ensuring that the fuel cell power at both the initial and final time steps is maintained at the minimum level of 10 kW.

The state of charge expression for the battery (SoC_{batt}) derived from [19], is given in Eq. (7):

$$SoC_{batt}(t) = SoC_{batt}(t-1) - \frac{P_{batt}(t) \bullet \Delta t}{E_{batt,rated}} \tag{7}$$

where $P_{batt}(t)$ represents the battery power as a function of time (positive indicates discharging), Δt is the time interval between successive measurements (5 min), and $E_{batt,rated}$ is the rated capacity of the battery, which is 60 kWh [29].

The constraints for the battery system are defined in Eqs. (8)–(11):

$$C_{rate,min} \leq C_{rate}(t) \leq C_{rate,max} \tag{8}$$

$$P_{batt}(t) = C_{rate}(t) \bullet E_{batt,rated} \tag{9}$$

$$SoC_{batt,min} \leq SoC_{batt}(t) \leq SoC_{batt,max} \tag{10}$$

$$SoC_{initial} = SoC_{final} \tag{11}$$

The $C_{rate}(t)$ is constrained between −1 and 1, as specified in the system datasheet [29]. To minimize degradation, SoC_{batt} is maintained within the 20–80% range, as recommended by the manufacturer [29]. The $SoC_{initial}$ and SoC_{final} are set to 50%, ensuring energy balance without requiring shore charging. Consequently, the net battery contribution ratio accounting for the total charge and discharge power over the voyage should approach zero.

The power supplied by the system must match the demand at each time step, as shown in Eq. (12):

$$N_{FC} \bullet P_{FC}(t) + N_{batt} \bullet P_{batt}(t) = \frac{P_{diesel}(t)}{\eta_{conv} \bullet \eta_{inv} \bullet \eta_m \bullet \eta_{gb}} \tag{12}$$

where:

- N_{FC} and N_{batt} are the number of fuel cells and batteries respectively (design variables).
- $P_{FC}(t)$ and $P_{batt}(t)$ are the control variables. The total fuel cell power is equally distributed to all fuel cells and the total battery power is equally shared across all batteries.
- $P_{diesel}(t)$ is the original diesel engine power output as a function of time (for the direct-drive propulsion system).
- $\eta_{conv}, \eta_{inv}, \eta_m, \eta_{gb}$ are the efficiencies of converters, inverter, propulsion motor and gearbox respectively, required for the retrofitted hydrogen-based powertrain. The shaft efficiency and the controllable pitch propeller efficiency are assumed to be the same in the original and the new design.

The analysis includes the unidirectional fuel cell converters and the bidirectional battery converters. Each power supply component is assigned a dedicated converter, as expressed in Eqs. (13) and (14):

$$N_{FC} = N_{FC,conv} \tag{13}$$

$$N_{batt} = N_{batt,conv} \tag{14}$$

3.2.2. System placement

The placement of systems within the existing engine room space must comply with guidelines and regulations set by the classification societies [30,31]. Additionally, hydrogen-based general arrangements from other ships are referenced to guide the conceptual retrofitting of the case vessel [32].

The fuel cells are split symmetrically into two rooms (port and starboard), separated by a gastight bulkhead, in compliance with safety regulations [30,31]. If one room is isolated after a fault, the other room can still supply power. The battery systems are placed in a dedicated space, adjacent to the fuel cell room. To enhance safety and system reliability, the converter room and the propulsion motor room (including inverter, motor and gearbox) are separated, ensuring that a failure in the main electrical distribution system does not result in complete propulsion loss.

The fuel cells, batteries and converters can be stacked in vertical groups. The lowest unit in any stack is positioned at a vertical distance of 1 m above the keel, based on the general arrangement of the vessel, and each stack can contain up to five units. This allows sufficient vertical clearance with enough space to lift out the top unit for maintenance or replacement. All engine room compartments are designed with sufficient space for access, inspection, and maintenance, allowing for easy removal and replacement of degraded or malfunctioning components.

A set of predefined feasible positions (slots) within the engine room, based on regulations and other general arrangements [30–32], is used as input to the optimization model. Each component has x (longitudinal distance from the aft perpendicular), y (transverse distance from the centerline), and z (vertical distance from keel) coordinates. The optimization model searches over many feasible layouts and selects which slots to use for the required number of components to satisfy ship stability constraints. The engine room layout and system arrangement will be presented in the results, at Section 4.2.1.

To meet the vessel's energy requirements and space constraints, liquefied hydrogen (LH_2) is selected as the fuel storage method. Type C, cylindrical LH_2 tanks are used due to their ease of construction and lower cost compared to other designs such as circular [33]. The tank volume, weight, and diameter are calculated as shown in Eqs. (15)–(17):

$$v_{LH_2,tank} = F_{total} \bullet N_{trips,refuel} \bullet v_{spec} \bullet f_{margin,tank} \tag{15}$$

$$w_{LH_2,tank} = F_{total} \bullet N_{trips,refuel} \bullet w_{spec} \bullet f_{margin,tank} \tag{16}$$

$$D_{LH_2,tank} = \sqrt{\frac{4 \bullet v_{LH_2,tank}}{\pi \bullet L_{LH_2,tank}}} \tag{17}$$

where:

- $v_{LH_2,tank}$ is the volume of the LH_2 tank (m^3).
- $w_{LH_2,tank}$ is the weight of the LH_2 tank (kg).
- $N_{trips,refuel}$ is the number of trips before refuelling. This parameter affects the tank size and thus the ship stability.
- $v_{spec} = 0.0248$ m^3/kg, is the volumetric specification of the LH_2 tank [34].
- $w_{spec} = 8.7$ kg/kg, is the gravimetric specification of the LH_2 tank [34].
- $f_{margin,tank} = 1.4$, is the LH_2 tank margin factor, used to account for reduced filling limits (60%) due to thermal expansion and lifetime increase in fuel consumption due to system degradation, based on regulations [35].
- $D_{LH_2,tank}$ is the diameter of the LH_2 tank (m).
- $L_{LH_2,tank}$ is the length of the LH_2 tank (m).

The LH_2 tank is placed on the open deck between the superstructure and cargo hold to reduce the risks associated with leaks, allowing hydrogen to disperse in the atmosphere. According to regulations, the LH_2 tank should be placed at least 20% of the vessel's breadth away from the side shell plating to prevent damage from side collisions [30]. It is oriented transversally in symmetry with the centerline to minimize the sloshing effect. Thus the maximum tank length should not exceed 7.5 m. The maximum available volume for the tank placement at the upper deck is 212 m^3 without obstructing visibility from the bridge.

3.2.3. Ship stability constraints

The vessel originally used a direct-drive diesel propulsion system. For the hydrogen retrofit, the main diesel engine (11.6 tons) and 275 tons of diesel fuel, with a Vertical Center of Gravity (VCG) of 4.1 m, are removed. Furthermore, the original design required 28 tons of ballast to satisfy the stability requirements, which are recalculated for the new design. The diesel fuel tanks are structurally integrated at the bottom and sides of the vessel. Most of the original diesel fuel tanks remain unused in the hydrogen-based design. These spaces could potentially be repurposed for ballast or cargo storage. However, this would require significant structural modifications and detailed engineering assessments, which are beyond the scope of this study.

For the VCG assessment, the masses and vertical moments of the removed items are subtracted and those of the new hydrogen components are added. The reduction in weight by removing 275 tons of diesel fuel significantly alters the weight distribution.

The main added components/parameters in the new design are summarized below:

- Fuel cells (primary energy source).
- Batteries (low-load support and peak-shaving).
- Converters, inverters, DC switchboard and propulsion motor.
- Gearbox.
- LH_2 tank and hydrogen fuel.
- Ballast to satisfy stability requirements.

To minimize additional investment costs and maintain efficiency under varying load conditions, the original controllable pitch propeller is retained in the hydrogen-powered design.

In the event of a major failure in the hydrogen-based system, the vessel has an emergency diesel generator located in a dedicated compartment at the aft end of the superstructure.

As stated in [32], a weight margin factor of 2% of original lightship (23.4 tons) is applied in the retrofitted design to account for increased weight due to:

- Structural reinforcements required for the integration of hydrogen storage tank and fuel cell systems.
- Additional auxiliary and safety systems (ventilation, fire suppression etc.) necessary for compliance with operational and regulatory standards.

The new total weight of the vessel after the removal and the addition of the necessary systems is computed as shown in Eq. (18):

$$W_{new,total} = W_{original} - W_{removed} + W_{added} \tag{18}$$

The total new weight ($W_{new,total}$) is constrained to remain within ± 5% of the original total weight of the diesel-based version with the use of the required amount of ballast. This ensures that the retrofitted and original designs maintain similar hydrodynamic resistance and propulsive power requirements.

The following equations and constraints are related to ship stability analysis. The Vertical Center of Gravity of each component (VCG_i) is the distance from its geometric center to the keel of the vessel and the total VCG is calculated based on the ratio of the sum of contributions of the vertical moments and weights (w) of the systems, as shown in Eq. (19):

$$VCG = \frac{\sum_i (w_i \bullet VCG_i)}{\sum_i (w_i)} \tag{19}$$

According to the stability booklet of the case ship, the total VCG of the vessel should not exceed 5.044 m.

When a vessel's tank (fresh water, ballast, hydrogen etc.) is partially filled, the liquid's movement causes a virtual rise in the VCG, impacting stability. This free surface moment (FSM) effect is calculated using Eq. (20):

$$FSM_{tank} = I_{tank} \bullet \rho \tag{20}$$

where:

- I_{tank} is the transverse moment of inertia of a tank (m^4).
- ρ is the liquid density (ton/m^3).

For the retrofitted design FSM_{new} is computed as shown in Eq. (21):

$$FSM_{new} = FSM_{original} - FSM_{diesel} + FSM_{LH_2,tank} + FSM_{ballast} - FSM_{ballast,removed} \tag{21}$$

where:

- $FSM_{original}$ is the total FSM of the diesel-based version.
- FSM_{diesel} is the FSM contribution from the removed diesel fuel.
- $FSM_{LH_2,tank}$ is the FSM effect from the added hydrogen fuel.
- $FSM_{ballast}$ is the FSM contribution of the additional ballast required in the new design to ensure compliance with the stability regulations. To minimize FSM effects, ballast tanks are assumed to remain fully filled throughout the voyage.
- $FSM_{ballast,removed}$ is the FSM contribution of removed ballast from the original design.

The FSM for a half-filled cylindrical LH_2 tank is calculated using Eqs. (22) and (23):

$$FSM_{LH_2,tank} = I_{LH_2,tank} \bullet \rho_{LH_2} \tag{22}$$

$$I_{LH_2,tank} = \frac{1}{12} \bullet D^3_{LH_2,tank} \bullet L_{LH_2,tank} \tag{23}$$

The virtual rise in VCG (GG') captures the effect of FSM on the VCG. It is computed as shown in Eq. (24):

$$GG' = \frac{FSM_{new}}{W_{new,total}} \tag{24}$$

In the homogeneously loaded condition, additional ballast can be placed in the existing water ballast tanks of the vessel. To prevent excessive heeling moments, ballast is distributed symmetrically in the transverse direction, with one tank on the port side and another on the starboard side. To determine the optimal ballast configuration, various tank placement combinations along the vessel's length are evaluated. The inclusion of ballast configuration selection introduces a combinatorial aspect to the optimization problem, as it requires the evaluation of discrete combinations of ballast arrangements (amount and position of ballast required to satisfy stability constraints).

The longitudinal center of gravity (LCG) is a key parameter in assessing the trim of the retrofitted vessel. It is measured from the aft perpendicular, and can be computed as shown in Eq. (25):

$$LCG = \frac{\sum_i (w_i \bullet LCG_i)}{\sum_i (w_i)} \tag{25}$$

The trim (m) represents the difference between vessel's aft and forward drafts, and is calculated using Eq. (26):

$$Trim = \frac{(LCG - LCB) \bullet W_{total}}{MCT \bullet 100} \tag{26}$$

where:

- LCB is the longitudinal center of buoyancy (m),
- W_{total} is the total displacement of the vessel (tons),
- MCT is the moment to change trim (ton • m/cm).

The vessel is designed to operate at specific trim values to minimize hydrodynamic resistance and fuel consumption. Although IMO regulations do not specify mandatory trim constraints, maintaining a trim deviation within ± 0.05 m from the original design, as shown in Eq.

(27), can be critical for optimal performance.

$$\left|Trim_{new} - Trim_{original}\right| \leq 0.05\,(\mathrm{m}) \tag{27}$$

The original trim value in the homogeneous loaded condition is −0.42 m, where the negative sign indicates a trim by stern. The LCB and MCT values are derived from the hydrostatic data in the vessel's stability booklet. For the retrofitted hydrogen-based design, they are obtained using linear interpolation, within the optimization framework, based on the new displacement $W_{new,total}$.

The following stability constraints in Eqs. (28)–(33) based on IMO regulations, must be satisfied for the case vessel. These constraints apply to both the original and the retrofitted design:

$$GM = KM - VCG > 0.3\,(\mathrm{m}) \tag{28}$$

$$GZ_{max} > 0.2\,(\mathrm{m}) \tag{29}$$

$$\varphi(GZ_{max}) > 25\,(^{\circ}) \tag{30}$$

$$Area_{GZ:(0^{\circ}-30^{\circ})} > 0.055\,(\mathrm{m} \bullet \mathrm{rad}) \tag{31}$$

$$Area_{GZ:(0^{\circ}-40^{\circ})} > 0.090\,(\mathrm{m} \bullet \mathrm{rad}) \tag{32}$$

$$Area_{GZ:(30^{\circ}-40^{\circ})} > 0.030\,(\mathrm{m} \bullet \mathrm{rad}) \tag{33}$$

where:

- GM is the distance between the vessel's center of gravity and its transverse metacenter (a virtual point where the vertical lines of upright and heeled centers of buoyancy intersect). GM represents the initial stability of the vessel and it should be at least 0.3 m for sufficient transverse stability.
- KM is the distance between the keel of the vessel and its transverse metacenter. KM is determined from the hydrostatic tables similar to LCB and MCT, and it depends on the ship's hull shape and displacement.
- GZ righting arm is the horizontal distance between the vessel's center of gravity and the vertical line passing through the center of buoyancy when the ship is heeled at an angle φ.

The GZ at a certain heeling angle φ is determined using Eq. (34):

$$GZ(\varphi) = (KN - VCG) \bullet \sin(\varphi) \tag{34}$$

where:

- the $KN\sin(\varphi)$ values from the cross curves of stability represent the horizontal lever from the keel to point N, the intersection of the buoyant-force line with the ship's centerline plane.

The $KN\bullet\sin(\varphi)$ values are provided in the stability booklet of the case vessel for various displacements at the heeling angles of 0, 2, 5, 10, 12, 15, 20, 30, 40, 50, and 60 degrees. Linear interpolation can be performed similarly to KM, LCB and MCT to obtain the KN values at the corresponding displacements.

The GZ-φ curve is a graphical representation of ship's stability characteristics at different heeling angles. The IMO has imposed constraints for certain areas under the GZ curve (0°–30°, 0°–40°, and 30°–40°), as shown in Eqs. (31)–(33). These areas can be estimated using the trapezoidal rule [36]. This method approximates the integral of the function $GZ(\varphi)$ over an interval $[\varphi_i, \varphi_{i+1}]$. The total area under the curve over a set of n intervals is obtained by summing the contributions over each interval, as shown in Eq. (35):

$$Area_{GZ:(\varphi_1-\varphi_2)} = \frac{1}{2} \bullet \sum_{i=1}^{n} \left(\left(GZ(\varphi_i) + GZ(\varphi_{i+1}) \right) \bullet (\varphi_{i+1} - \varphi_i) \right) \tag{35}$$

where φ_i and φ_{i+1} are consecutive heel values (in radians) within the range of φ_1 to φ_2.

The stability constraints (VCG, trim etc.) are active constraints within the optimization framework. The model searches over many feasible layouts and selects positions for the components and ballast in order to satisfy these constraints.

3.2.4. Optimization objective function

The objective function to be minimized is the total lifetime cost which consists of:

- Capital expenditure (CAPEX) – the initial investment cost.
- Net present value of operational expenditures (NPV_{OPEX}) – discounted to account for the time value of money over the vessel's lifetime.

The relationship is expressed mathematically as shown in Eq. (36):

$$\begin{matrix} \min(CAPEX + NPV_{OPEX}) \\ (N_{FC}, N_{batt} P_{FC}(t), P_{batt}(t)) \end{matrix} \tag{36}$$

The CAPEX is calculated as shown in Eqs. (37)–(39):

$$CAPEX = CAPEX_{systems} + CAPEX_{tank} \tag{37}$$

$$CAPEX_{systems} = \sum_{systems} (N_{system} \bullet P_{system,rated} \bullet C_{system}) \tag{38}$$

$$CAPEX_{tank} = F_{total} \bullet N_{trips,refuel} \bullet f_{margin,tank} \bullet C_{tank} \tag{39}$$

where.

- *system* refers to engine room main components (fuel cells, batteries, converters, inverter, motor, gearbox).
- N_{system} is the number of units for each system.
- $P_{system,rated}$ is the rated power (kW).
- C_{system} is the investment cost per unit capacity ($/kW).
- C_{tank} is the tank cost per unit mass of stored LH_2 ($/kg).

Eq. (39) links the LH_2 tank CAPEX to the required mass of hydrogen stored onboard between refuelling events, $F_{total} \bullet N_{trips,refuel}$, adjusted by $f_{margin,tank}$ to account for reduced filling limits and lifetime increase in fuel consumption. The resulting required stored hydrogen mass is multiplied by C_{tank} ($/kg LH_2 stored) to obtain the tank capital cost. This formulation ensures that the tank CAPEX scales directly with the hydrogen storage requirement.

The CAPEX values for the components are derived from the authors' previous study [25].

Ref [25] documents the full cost methodology, source breakdown, and applicable reference years for each cost input. Depending on the component, cost values are taken from peer-reviewed literature, industry/vendor data, or forward-looking projections from energy-transition reports. Therefore, reference years difference across cost items. Uncertainty in rapidly changing costs (e.g., hydrogen price) is handled through sensitivity analysis in this study.

The NPV of operational costs includes fuel expenses, maintenance and component replacement costs over the vessel's remaining lifetime after retrofitting. It is calculated using Eq. (40):

$$\begin{aligned} NPV_{OPEX} = \sum_{t=1}^{T} \Bigg(& \left(\frac{F_{annual_t} \bullet C_{h_2}}{(1+r)^t} \right) + \left(\frac{b_{FC,replace_t} \bullet N_{FC} \bullet P_{FC,rated} \bullet C_{FC,replace}}{(1+r)^t} \right) \\ & + \left(\frac{b_{batt,replace_t} \bullet N_{batt} \bullet E_{batt,rated} \bullet C_{batt,replace}}{(1+r)^t} \right) \\ & + \left(\frac{\Sigma(C_{system,maint_t})}{(1+r)^t} \right) \Bigg) \end{aligned} \tag{40}$$

where:

- F_{annual} is the annual fuel consumption (kg/year).

- C_{h_2} is the hydrogen price with a baseline value of 6$/kg [25].
- $r = 5\%$ is the interest rate [25].
- t is the time index (in years).
- $T = 20$ years is the remaining lifetime of the vessel after retrofitting.
- $b_{FC,replace,t}$ is the binary variable for fuel cell replacement in year t. According to the manufacturer, the fuel cells are replaced after 20,000 operating hours [26,37].
- $b_{batt,replace,t}$ is the binary variable for battery replacement in year t. The batteries are assumed to be replaced every 7 years based on the authors' previous study [25].
- $C_{FC,replace}$ and $C_{batt,replace}$ ($/kW) are the replacement costs for fuel cells and batteries respectively, which are assumed to be 50% of their initial CAPEX, based on projected cost reductions due to technological advancements and increased market adoption [25].
- $C_{system,maint_t}$ ($/kW/year) is the annual maintenance cost of each system, obtained from [25].

The annual fuel consumption is initially determined based on the total fuel consumption per trip and the number of trips per year, as shown in Eq. (41):

$$F_{annual} = F_{total} \bullet N_{trips,annual} \tag{41}$$

The number of annual trips ($N_{trips,annual}$) is 200, with the power demand data of 100 sailing days, from Fig. 2, repeated twice every year.

To capture the effects of fuel cell degradation and hydrogen boil-off losses, the fuel consumption is calculated annually using a boil-off loss factor (b_{h_2}) and a degradation factor (d).

A 0.2% daily loss of stored hydrogen due to boil-off is assumed, based on [38]. For the boil-off factor (b_{h_2}), the cumulative hydrogen loss per refuelling cycle is calculated (i.e., how much hydrogen is lost, relative to the initial amount, until refuelling). To simplify the model, a constant boil-off factor is assumed over time, under the assumption that periodic tank inspections and regular insulation upgrades mitigate long-term changes in boil-off rates.

The degradation factor (d) is derived from the relationship between voltage drop and fuel consumption increase. The nominal cell voltage is 0.7 V, and the fuel cell replacement occurs when the voltage drops by 10% from its nominal value [8]. Fuel cell degradation is represented using a simplified lifetime-based approach rather than a detailed physics-based model. This avoids relying on degradation coefficients reported in the literature that are primarily derived from automotive operating conditions (e.g., Ref. [39]) and may lead to unreliable results for maritime operation. The fuel cell is assumed to experience a total voltage drop of 10% over its operational lifetime [8], at which point replacement occurs according to the manufacturer provided lifetime limits (20,000 operating hours), corresponding to approximately 4 years under the considered operational profile. The total voltage drop is therefore distributed uniformly over the replacement interval, and the annual voltage drop, ΔV_{annual}, is calculated as the total allowable voltage drop divided by the number of years until replacement (Eq. (42)). This constant annual voltage drop is then used to approximate the annual increase in fuel consumption due to degradation, which is a critical contributor to total lifetime cost.

$$\Delta V_{annual} = \frac{\Delta V_{total}}{Y_{replace}} \tag{42}$$

where:

- $\Delta V_{total} = 10\% \bullet 0.7 = 0.07$ V is the total voltage drop.
- $Y_{replace}$ is the number of years until replacement.

This lifetime-based degradation formulation is used only in the lifetime cost model and is distinct from the transient load-based degradation proxy used in Section 3.1 to assess the representativeness of the reduced power profiles.

Fuel cell efficiency, η_{FC}, is directly proportional to its operating voltage, as defined by [40] and shown in Eq. (43):

$$\eta_{FC} = \frac{V_{cell}}{V_{reversible}} \tag{43}$$

where:

- $V_{cell} = 0.6$–0.8 V, is the actual cell operating voltage [26].
- $V_{reversible} = 1.23$ V is the theoretical reversible voltage under ideal conditions.

Since hydrogen consumption is inversely proportional to the efficiency, at a given power output, the annual increase in fuel consumption due to degradation can be approximated as shown in Eq. (44):

$$\frac{\Delta F}{F_{annual,initial}} \cong \frac{\Delta V_{annual}}{V_{cell,nominal}} \tag{44}$$

where:

- ΔF is the annual increase in fuel consumption
- $F_{annual,initial}$ is the initial annual fuel consumption
- $V_{cell,nominal} = 0.7$ V is the nominal cell voltage.

Thus, the degradation factor (d) is obtained from Eq. (45):

$$d = 1 + \frac{\Delta F}{F_{annual,initial}} \tag{45}$$

The annual fuel consumption over the vessel's operational lifetime (T) is computed iteratively, incorporating both boil-off losses and degradation effects, as shown in Eq. (46):

$$F_{annual_t} = F_{annual_{t-1}} \bullet (1 + b_{h_2}) \bullet d \tag{46}$$

After fuel cell replacements, the annual fuel consumption is reset to its original value.

This approach ensures that the model dynamically captures the combined effects of fuel cell degradation and boil-off losses while maintaining realistic operational assumptions regarding fuel cell lifespan and system replacements.

The key model variables and parameters for the cost optimization and stability analysis are summarized in Table 1.

3.2.5. Optimization solver

The framework is a MINLP optimization with combinatorial aspects that is solved using the SCIP solver.

- Mixed-integer: binary, integer, and continuous variables for decision making.
- Nonlinear: Bilinear terms with the product of design and control variables introducing non-convexity (Eqs. (2) and (12)).
- Combinatorial: Discreet selection of configurations from a set of predefined feasible positions (slots) (system placement in the engine room, and selection of ballast amount and position to satisfy stability constraints).

SCIP is an open-source solver developed for MILP and MINLP problems. It is used in this study to manage the complexity of the optimization problem and provide high-quality solutions. SCIP solves MINLPs to global optimality using a spatial branch-and-bound algorithm, which combines branch-and-infer and branch-and-cut methods [41]. The key techniques utilized by SCIP include:

- Pre-solving: Simplifies the problem (to improve computational efficiency) by removing redundant variables and constraints, and tightening bounds.
- Branch-and-bound exploration: Divides the problem into smaller subproblems by branching on variables. Each subproblem is solved

Table 1
Main optimization parameters.

Design/control variables and cost parameters	
N_{FC}	Number of fuel cells – design variable
N_{batt}	Number of batteries – design variable
P_{FC}	Fuel cell power – control variable (kW)
P_{batt}	Battery power – control variable (kW)
SoC_{batt}	Battery state of charge (%)
F_{total}	Voyage fuel consumption (kg)
$N_{trips,annual}$	Number of annual trips
$CAPEX$	Capital expenses ($)
NPV_{OPEX}	NPV of Operational Expenses ($)
C_{system}	System cost per unit ($/kW)
$C_{FC,replace}$	Fuel cell replacement cost ($/kW)
$C_{batt,replace}$	Battery replacement cost ($/kW)
$C_{system,maint}$	System maintenance cost ($/kW/year)
C_{h2}	Green hydrogen price ($/kg)
b_{h2}	Boil-off factor
d	Degradation factor
System placement and stability variables	
x,y,z	Component / ballast coordinates (m)
$N_{trips,refuel}$	Number of trips before refueling
$D_{LH2,tank}$	Diameter of hydrogen tank (m)
w	weight of each system (kg)
VCG	Vertical center of gravity (m)
FSM	Free surface moment (ton m)
GG'	Virtual rise in VCG (m)
GM	Metacentric height (m)
KM	Keel-to-metacenter distance (m)
GZ	Righting lever (m)
φ	Heeling angle (°)
LCG	Longitudinal center of gravity (m)
LCB	Longitudinal center of buoyancy (m)
MCT	Moment to change trim (ton m/cm)
$Trim_{new}$	Trim of new design (m)

using linear or nonlinear relaxations to compute dual bounds, guiding the search toward the optimal solution.
- Cutting planes: Adds linear or nonlinear cuts to eliminate infeasible or suboptimal regions, tightening the relaxation and reducing the search space.
- Heuristics: Uses primal heuristics to quickly identify good feasible solutions, reducing the optimality gap and accelerating convergence.

During the solution process, SCIP continuously updates the primal bound (best feasible solution found up to a certain point) and the dual bound (best possible solution from relaxations). Convergence is achieved when the difference between the two (optimality gap) is zero, which indicates that the optimal solution has been found. In this study, SCIP was run with a 0% optimality-gap termination criterion.

Heuristic and metaheuristic solvers such as genetic algorithms are widely used for the optimal design of ship energy systems [19]. These methods rely on stochastic processes and can provide good solutions but without any guarantee of global optimality. They often require extensive computational resources and fine-tuning to achieve satisfactory results. Unlike heuristic methods, SCIP uses a branch-and-bound algorithm that enables effective exploration of the solution space without excessive computational demands, making it a reliable choice for this application [41].

4. Results and discussion

4.1. Power profile analysis results

The representative load profile, shown in Fig. 3, was synthesized using the probability-based profile generation method.

To enable direct comparison with the full annual dataset, the reduced profile was scaled up using the downsampling factor to ensure both profiles cover the same duration. The resulting deviations are

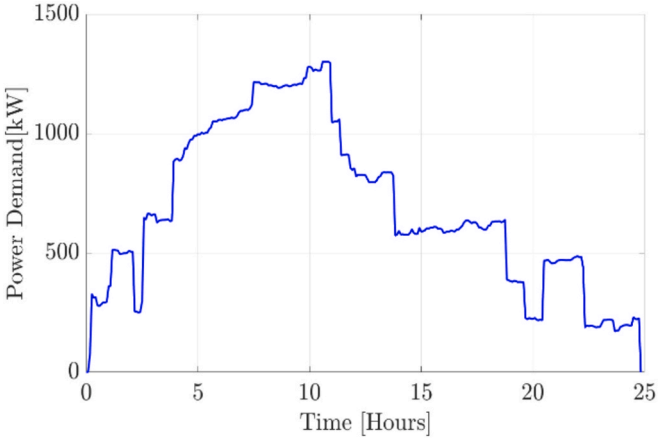

Fig. 3. Representative profile generated using the probability-based profile generation method.

0.33% in fuel consumption and 4% in fuel cell degradation relative to the annual profile, both within the ± 5% acceptance threshold.

Due to the stochastic nature of the sampling procedure, the profile generation was repeated ten times, and the reduced one-day profile shown in Fig. 3 was selected based on minimal deviations from the full annual dataset. This representative profile is subsequently used in the lifetime cost optimization.

Appendix B provides the corresponding power distribution and load ramp statistics for the annual and reduced profiles, supporting interpretation of the profile representativeness.

4.2. Energy system topology and lifetime cost optimization results

Subsection 4.2.1 focuses on the system selection and arrangement, and subsection 4.2.2 presents the optimization (cost and stability) results. Finally, in Subsection 4.2.3, alternative design arrangements are discussed.

4.2.1. System selection and placement

The selected 100-kW proton exchange membrane fuel cell stack operates within an efficiency range of 48–62% and exhibits high specific power and power density compared to other fuel cells [26,37]. At the beginning of life, the peak power output of the stack is 120 kW. Over its operational lifespan, degradation leads to a 17% reduction in peak power, resulting in a rated power of 100 kW at the end of life [26,37].

The variable fuel cell output voltage requires regulation via DC-DC converters to ensure stable integration with the ship's power system [42]. For compatibility between fuel cells and converters, the output voltage and current ranges of the fuel cell must align with the input specifications of the unidirectional converter. The converters must regulate the output voltage to the DC bus level of 700 V. The same fuel cell and converter systems were utilized in the conceptual design of a hydrogen fuelled ferry [37,43]. According to Bye et al. [43], the lowest recorded converter efficiency at end-of-life conditions was 98.2%. Therefore, a DC-DC converter efficiency of 98.5% is assumed in this study.

A 60-kWh lithium–iron phosphate battery pack, with a nominal output voltage of 576 V, is selected for low-load support and peak-shaving [29]. The same DC-DC converter hardware can be used in unidirectional mode for the fuel cells and in bidirectional mode for the batteries, allowing onboard charging from excess fuel cell power [42].

The 700-V DC switchboard distributes current from power sources to consumers via converters and inverters [44]. It consists of: the main busbars, bus-tie breaker, connection points for power supply and consumer modules, circuit breaker, fuses, and additional control/monitoring equipment.

The DC-AC converter (inverter), also referred to as variable frequency drive, converts DC power from the switchboard into AC power for the electric propulsion motor. A 1400-kW AC induction motor (AMI 500L8W) is selected to cover the peak propulsive power demand (Fig. 3), and an additional margin for increased power demand [45]. Based on the representative load profile (Fig. 3) and the equipment specifications, the motor is expected to operate with an average efficiency of 96% [45].

A 1400 kW inverter (ACS880-104LC) is selected for motor control, with an average efficiency of 98.5% [46]. The inverter and motor nominal voltages are matched at 690 V. The inverter's nominal output current exceeds the motor's current, ensuring its capability to operate under full-load conditions. The inverter also supports frequency control of 50 Hz, with potential variations depending on the inverter settings.

A gearbox is required to match the propeller's rotational speed with the motor's output speed. At the most frequent operating speed range of 9–11 knots, the controllable pitch propeller operates at 110–150 revolutions per minute (rpm). To achieve compatibility, the gearbox must reduce the motor speed from 750 rpm to approximately 130 rpm, requiring a reduction ratio of 5.76. A continuous- duty gearbox (MGN 2026 V) rated at 1489 kW, with a 6:1 reduction ratio is selected to align the motor and propeller speeds [47]. A gearbox efficiency of 98% is assumed based on [48].

The optimization model was solved with the SCIP solver, achieving a 0% optimality gap. The optimal propulsion system design consists of 14x100 kW fuel cells and 3x60 kWh batteries. The final retrofitted configuration, including all the main systems and their locations within the engine room compartments, is shown in Fig. 4.

The portable water tanks are positioned at the sides of the vessel, outside the illustrated machinery compartments, as per the original design.

Green boxes with 'X' represent positions available for placement that were not chosen by the optimization model. All other boxes contain the number of units that are placed in the specific positions for each system category (fuel cells, batteries, converters etc.).

Each fuel cell room contains seven modules, separated by a gastight bulkhead. The fuel cells are arranged symmetrically about the centerline and stacked vertically in groups of up to five units. The three battery modules are located in a dedicated compartment adjacent to the fuel cell rooms and positioned along the centerline ($y = 0$) to minimize transverse moment effects. The fuel cell converters and battery converters are located in the electrical machinery room. The inverter, motor, and gearbox are installed in the propulsion room. Some of the fuel cells and fuel cell converters are arranged in five-module vertical stacks, highlighting their limited influence on the vessel's vertical stability. Auxiliary and safety-related equipment can be accommodated within separate compartments or in the remaining available spaces of the engine room.

Several propulsion system arrangements were evaluated before selecting the final configuration:

- Single motor-gearbox in-line with the propeller shaft and propeller – This is the simplest configuration incorporating the fewest number of components.
- Offset configuration with dual motor-dual gearbox perpendicular to a single propeller shaft – This configuration provides increased component redundancy but introduces shaft alignment challenges, motor synchronization issues, and limited engine room space.
- Dual-shaft, twin-screw, dual-motor-gearbox – This configuration offers maximum propulsion redundancy, but requires significant design modifications and detailed hydrodynamic analysis to retrofit the original single-shaft diesel-based design.
- Single shaft, dual-motor, single/dual gearbox configuration – This configuration limits the available horizontal engine room space and introduces complexities in motor synchronization.

The inline configuration with a single motor, gearbox, shaft and propeller was chosen due to its: simplicity, lower cost, reduced weight, ease of access and maintainability. This arrangement also provides sufficient space for auxiliary and safety equipment without introducing challenges related to motor synchronization and shaft alignment. Furthermore, propulsion system redundancy is not a primary design criterion, as the original diesel-based design utilized a similar configuration.

4.2.2. *Optimal cost and stability results*

The total lifetime energy system cost of the optimal design (14x100 kW fuel cells, and 3x60 kWh batteries) is estimated at 22.9$ million. The contributions of individual cost categories to the total cost are illustrated in Fig. 5.

Fuel cost is the dominant contributor to total lifetime cost, accounting for 74.2%. Since hydrogen consumption is price-inelastic for the selected configuration, total lifetime cost scales proportionally with hydrogen price. Consequently, a ± x% change in hydrogen price leads to a ± 0.742x% change in total lifetime cost (e.g., a 50% increase in hydrogen price results in a 37.1% increase in total lifetime cost). Total CAPEX (including replacement costs) accounts for 24.5% of the total lifetime cost. The 'Other Systems CAPEX' category (shown in Fig. 5) includes investment costs for converters, inverter, motor and gearbox. The battery system and the total maintenance costs of all systems contribute minimally to the total lifetime cost.

The optimal power distribution between the fuel cells and the batteries is shown in Fig. 6.

At the beginning and end of the voyage, the batteries are charged using excess fuel cell power, since the fuel cells cannot operate below

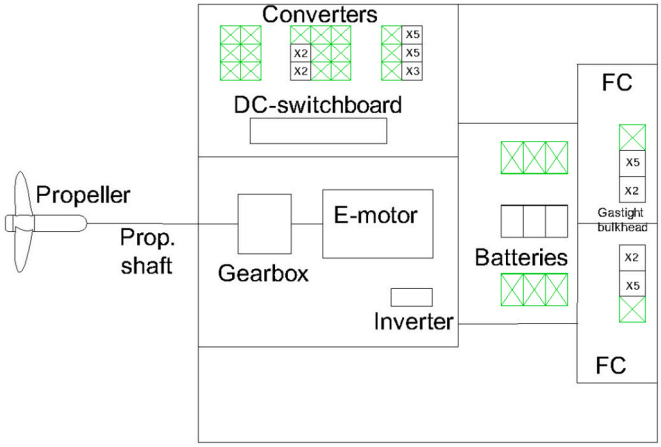

Fig. 4. Engine room layout for the optimal propulsion system design.

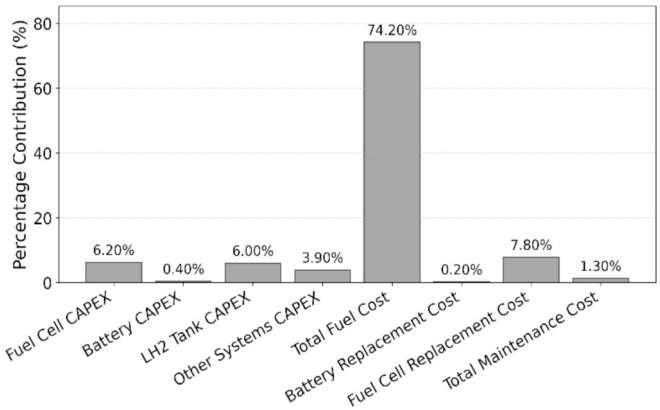

Fig. 5. Cost contributions to total lifetime cost.

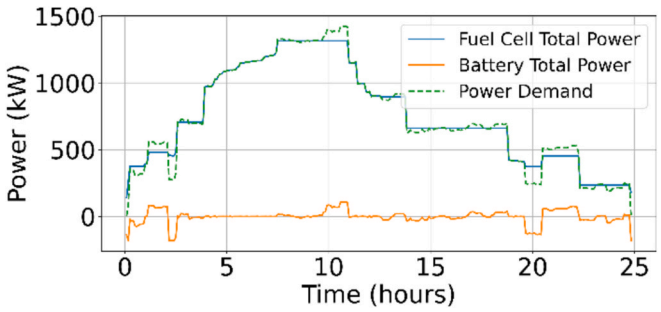

Fig. 6. Optimal power distribution between fuel cells and batteries.

10% of their rated power. Throughout the voyage, the fuel cells provide the majority of the power demand, while the batteries are mainly used for low-load support and peak shaving. At the end of the voyage, the battery is charged back to 50%, as shown in Fig. 7, to avoid shore charging due to limited available infrastructure.

The total fuel consumption, F_{total}, after retrofitting, is 1049.3 kg/trip. The annual fuel consumption variations, including fuel cell degradation and boil-off effects are depicted in Fig. 8. There is a 2.5% annual increase in fuel consumption due to fuel cell degradation, and a 0.8% increase in the required hydrogen consumption due to cumulative boil-off per refuelling cycle. The annual hydrogen consumption is increased until the ends of years 4, 8, 12, 16 and 20, and then, after the fuel cell replacements, the fuel consumption is reset to its initial value at years 5, 9, 13, and 17.

The LH_2 tank is placed at the open deck with a VCG of 10.5 m. It weighs 51.1 tons, and its volume is 146 m^3, with a diameter of 4.97 m. With this tank size, the vessel requires refuelling every 4 sailing days (voyages). Furthermore, there is sufficient space at the upper deck for equipment inspection and maintenance. To satisfy the trim and vertical stability constraints, the vessel requires 171.5 tons of ballast with a VCG at 0.53 m and an LCG of 26.67 m. The total weight of the main engine room components in the retrofitted design (fuel cells, motor etc.) is 15.3 tons which is only 3.7 tons higher than the original diesel engine. After retrofitting, the vessel's total weight decreases by 1%, from 4835.8 tons to 4786.8 tons.

The LH_2 tank and the ballast placement significantly impact the vessel's stability, while the engine room components have minor effects due to their low weight compared to the total ship displacement. However, in ship designs with similar installed power but significantly smaller displacement (e.g., ferries), the positioning of engine room components is expected to have a more pronounced impact on stability.

The stability results for the homogeneous loaded departure condition (for the retrofitted design) are summarized in Table 2 and the GZ curve is shown in Fig. 9.

Table 2 presents the stability results for the homogeneous loaded departure condition, confirming compliance with the IMO intact stability criteria. The GZ curve and underlying area were validated against the original diesel-powered vessel to ensure minimal errors from the trapezoidal rule. Stability checks were also conducted for homogeneous

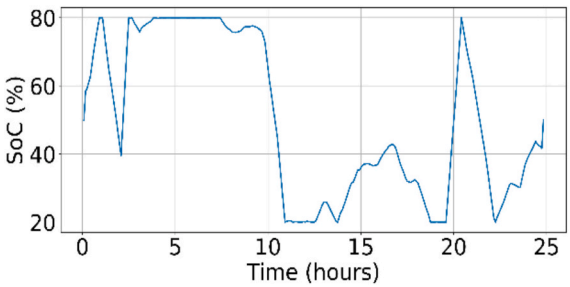

Fig. 7. Battery SoC.

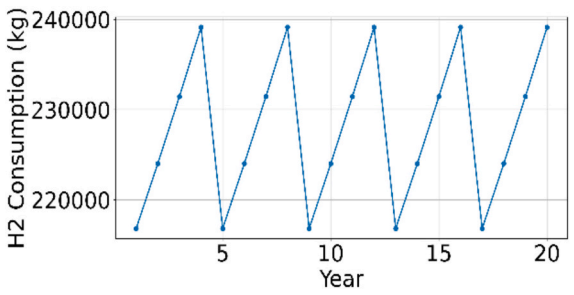

Fig. 8. Annual fuel consumption changes.

Table 2
Stability results for the retrofitted vessel.

Parameter	Value	Criterion
VCG	5.01 (m)	<5.044
GM	0.36 (m)	>0.3
GZ_{max}	0.55 (m)	>0.2
$\varphi(GZ_{max})$	50 (°)	>25
Area (0–30)	0.068 (m rad)	>0.055
Area (0–40)	0.136 (m rad)	>0.090
Area (30–40)	0.068 (m rad)	>0.030
$Trim_{new}$	−0.39 (m)	±5 cm

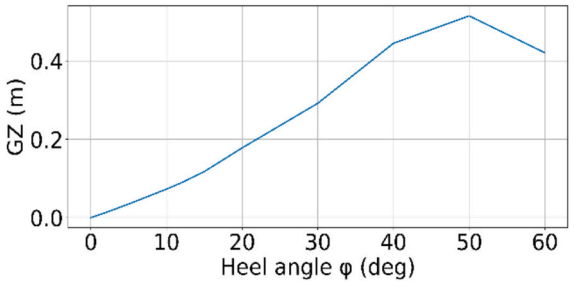

Fig. 9. GZ curve.

loaded arrival and ballast conditions to verify regulatory compliance. In the ballast departure condition the GM of the vessel is 1.74 m, which is much higher than the minimum of value of 0.3 m required by the regulations. The trim of the vessel can be adjusted in laden arrival, ballast departure and arrival conditions by rearranging the ballast.

4.2.3. *Alternative design arrangements*

The impacts of various design choices on the optimization results are analyzed below, to offer insights into alternative design considerations and arrangements.

Removing one fuel cell or one battery from the optimal design does not satisfy the optimization constraints (infeasible problem) due to insufficient energy supply at peak loads, and insufficient low-load support respectively. Adding one additional 100-kW fuel cell in the optimal design reduces fuel cost by 1.4% through more efficient operation at lower power levels, but increases CAPEX by 2.8%, resulting in a 0.06% rise in total lifetime cost. Incorporating an additional 60-kWh battery reduces fuel cost by 0.1%, but raises CAPEX by 1.1%, leading to a total cost increase of 0.19%. Further increases of system capacity result in higher total lifetime costs since the CAPEX increase outweigh the reductions in fuel consumption cost from more fuel-efficient operation at lower fuel cell power levels. From the above, further assurance can be obtained that the configuration of 14x100 kW fuel cells and 3x60 kWh batteries is the global optimum.

Placing a single LH_2 tank below the main deck could further improve stability by lowering the VCG. However, this would reduce available

cargo space by approximately 10% and require additional auxiliary systems, safety equipment, and structural reinforcements, thereby increasing total cost. Alternatively, dividing the hydrogen storage into two tanks could improve redundancy and reliability in case of failure. However, due to space constraints on the upper deck, one tank would need to be placed on the open deck and the other in the cargo space. This arrangement complicates design and auxiliary system integration, increases boil-off rates (due to smaller tank diameters), and raises total tank CAPEX [33,35]. Placing an LH2 tank below the open deck is a viable option for vessels with limited deck space and high VCG, such as containerships. For such designs, exploring different tank types and shapes could optimize fuel storage utilization [49].

5. Conclusions

This study presents a holistic framework for optimal ship system design and operation. The novelty of this work is that it incorporates a power profile analysis and synthesis method, energy system topology, ship stability, and lifetime cost minimization in a unified optimization framework. The original diesel mechanical propulsion system of a general cargo vessel is retrofitted with hydrogen fuel cells and batteries to lower its environmental footprint. Given the urgent need to decarbonize existing fleets to meet IMO emission targets, this study offers valuable insights into the retrofitting of conventional vessels with novel energy systems. Additionally, the versatility of the optimization model allows it to be adapted for the design of newbuild vessels with minimal modifications.

The following key results can be summarized:

- The probability-based profile generation approach produced a downsampled load profile with deviations of less than 5% in fuel consumption and fuel cell degradation compared to the original annual propulsive power data, enabling computationally efficient lifetime cost optimization with minimal loss of accuracy.
- The optimal configuration includes 14x100 kW fuel cells and 3x60 kWh batteries. The batteries support low-load operations and peak shaving, and they are charged from excess fuel cell power, without requiring shore charging. Oversizing either fuel cells or batteries was found to increase total lifetime cost, as the additional CAPEX outweighs fuel cost savings achieved through more fuel-efficient operation.
- The retrofitted design includes a single LH_2 tank (146 m^3, 4.97 m diameter) placed on the main deck with a VCG of 10.5 m, providing a range of 4 days without refuelling.
- The total ship weight of the retrofitted design is 1% lower than the original diesel-based version with the use of the necessary amount of ballast.
- The optimal retrofit satisfies all vertical stability and trim constraints using 171 tons of ballast at a VCG of 0.53 m and an LCG of 26.67 m in the homogeneous loaded condition. For this vessel, retrofit feasibility primarily depends on LH_2 storage sizing/placement, which directly determines ballast requirements. Engine-room components have a comparatively minor effect on vessel stability due to their low weight relative to ship displacement; several fuel cells and converters are arranged in five-module vertical stacks, highlighting their limited influence on vertical stability.
- The total lifetime cost of the optimal design is estimated at 22.9$ million, with a baseline fuel price of 6$/kg. Fuel costs have the largest contribution (74.2%) to total cost, while CAPEX (including replacements) accounts for 24.5%. Battery CAPEX and total maintenance costs together contribute less than 2% of the lifetime cost.
- Neglecting key real-world effects such as powertrain efficiency changes after retrofitting, degradation-driven increases in fuel consumption, and operating profile variability across routes can lead to non-robust designs and misleading lifetime cost outcomes.

Overall, these results demonstrate that cost-optimal and technically feasible solutions require the coupled consideration of system sizing, topology, operation, and stability constraints within a unified lifetime cost optimization framework. From a broader design and decision-making perspective, the results provide clarity on the feasibility of hydrogen-based ship retrofits under realistic technical and economic constraints. The viability of hydrogen-fuelled systems primarily depends on storage integration constraints and fuel price assumptions rather than power and propulsion system sizing alone. As such, the proposed framework supports informed assessment of when and under which conditions hydrogen-based ship energy systems become viable options for decarbonization, thereby supporting decision-making for maritime decarbonization strategies.

In future work, the impact of weather variability on the power profiles and lifetime cost can be investigated.

CRediT authorship contribution statement

Foivos Mylonopoulos: Writing – original draft, Visualization, Validation, Software, Methodology, Formal analysis, Conceptualization. **Andrea Coraddu:** Writing – review & editing, Visualization, Supervision, Methodology, Funding acquisition, Conceptualization. **Henk Polinder:** Writing – review & editing, Visualization, Supervision, Methodology, Funding acquisition, Conceptualization.

Declaration of competing interest

The authors declare that they have no known competing financial interests or personal relationships that could have appeared to influence the work reported in this paper.

Acknowledgments

This research was supported by the Sustainable Hydrogen Integrated Propulsion Drives (SH2IPDRIVE) project, which has received funding from RvO (reference number MOB21013) through the RDM regulation of the Ministry of Economic Affairs and Climate Policy.

Appendix A

Evaluation of an alternative RDP-based downsampling method

This appendix documents the evaluation of an algorithmic-based donwsampling approach that was investigated as a potential alternative to the probability-based method, but not adopted in the main analysis.

Overview of the RDP-based approach

As alternative to the probability-based profile generation method, a geometry-based downsampling approach using the Ramer Douglas Peucker (RDP) algorithm [26] was evaluated. The RDP algorithm simplifies a polyline (here, the power-time curve) by connecting the first and last points of a

segment with a straight line and computing the maximum perpendicular distance of the intermediate points to that line. If this maximum distance is below a prescribed tolerance ε, the intermediate points in that segment are discarded; otherwise, the farthest point is retained and the procedure is applied recursively to the two resulting subsegments. This recursive process continues until the maximum perpendicular deviation between the original polyline and each line segment is no greater than ε, resulting in a simplified polyline with fewer points that preserves the overall geometric shape of the original curve. Increasing ε reduces the number of retained points (and computational cost) but decreases fidelity to the original profile, so ε represents a trade-off between computational efficiency and approximation accuracy.

When applied to power profiles, the method produces a reduced representation with variable time steps while preserving the overall geometric shape. In this study, the original annual load profile was reduced from 30,000 data to 300 data (corresponding to a reduction factor of 100) using an ε value of 0.9. The resulting profile spans the same total operating duration but includes variable time steps ranging from 5 min to 51 h.

Performance with respect to fuel consumption and fuel cell degradation

The reduced profile obtained using the RDP algorithm was evaluated by comparing fuel consumption and fuel cell degradation estimates against those obtained from the full annual profile. The RDP-based reduction resulted in a deviation of −6.18% in fuel consumption, indicating that fuel consumption can be reasonably approximated despite the substantial reduction in dataset size.

In contrast the deviation in fuel cell degradation was −69%, demonstrating that the RDP algorithm fails to preserve transient load variations that are critical for degradation assessment. As illustrated in Fig. A1, the RDP-based reduced profile introduces significant power deviations at specific time intervals compared to the original profile.

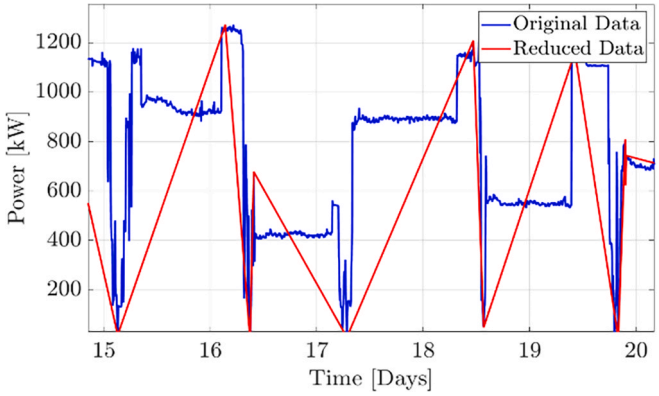

Fig. A1. RDP: Zoomed-in comparison of the profiles in the 1520 days period.

Rationale for exclusion from the main analysis

Due to its inability to accurately represent degradation-relevant dynamics, the RDP-based approach was not adopted for the generation of representative load profiles in this work. Achieving acceptable degradation estimates with the RDP would require a substantially larger number of retained data (in the range of thousands), which would significantly increase computational cost. Additionally, the variable time steps produced by RDP complicate integration with the subsequent optimization framework.

For these reasons, the probability-based method described in the main text was selected for all analyses presented in this study.

Appendix B

Power levels and load-ramp statistics for the probability-based profile generation method

Table B1 and Table B2 report selected descriptive statistics of the power levels and load ramps for the full annual profile and the representative profile generated using the probability-based method.

Table B1
Power level statistics (P10 and P90 denote the 10th and 90th percentiles of the power-level distribution).

Statistic (kW)	Annual profile	Representative profile
Mean power	696	685
P10-P90 power	349–917	220–1202
Max power	1284	1300

Table B1 summarizes the mean power, P10-P90 power range, and the maximum power level. The mean power of the representative profile differs by only 1.6% from that of the annual profile, which is consistent with the very small deviation observed in total fuel consumption (0.33%). The P10-P90 range indicates that the representative profile operates within a comparable power envelope. Differences in percentile bounds are expected due to the stochastic nature of the sampling procedure and the substantial reduction in dataset size.

Table B2
Load ramp statistics (P10 and P90 denote the 10th and 90th percentiles of the load-ramp distribution).

Statistic (kW)	Annual profile	Representative profile
Mean $\|\Delta P\|$	15.9	16.5
Median $\|\Delta P\|$	3	2.5
P10 – P90 $\|\Delta P\|$	0–30	0.5–25

Table B2 summarizes statistics of absolute power changes between successive time steps ($|\Delta P|$), including the mean, median and the P10-P90 ramp range. The close agreement in mean and median ramp magnitudes indicates that typical load-ramping behaviour is well presented in the reduced profile. The P10-P90 ramp range further confirms that the magnitude of common transient events is preserved, which is consistent with the small deviation observed in the degradation-related proxy (4%) used during profile selection.

The statistics presented in this appendix are provided for diagnostic purposes only. The representativeness of the reduced profile is assessed in the main text using deviations in fuel consumption and fuel cell degradation metrics (±5% acceptance threshold), rather than through direct matching of individual statistical descriptors.

Data availability

Data will be made available on request.

References

[1] Gritsenko D. Regulating GHG emissions from shipping: local, global, or polycentric approach? Mar Policy 2017;84:130–3. https://doi.org/10.1016/j.marpol.2017.07.010.

[2] International Maritime Organization. 2023 IMO strategy on reduction of GHG emissions from ships [Internet]. [cited 2025 Feb 10]. Available from: https://www.imo.org/en/ourwork/environment/pages/2023-imo-strategy-on-reduction-of-ghg-emissions-from-ships.aspx.

[3] United Nations Conference on Trade and Development. Review of maritime transport 2022 [Internet]. [cited 2025 Feb 13]. Available from: https://unctad.org/system/files/official-document/rmt2022_en.pdf.

[4] Fang S, Wang Y, Gou B, Xu Y. Toward future green maritime transportation: an overview of seaport microgrids and all-electric ships. IEEE Trans Veh Technol. 2020;69(1):207-219. Available from: https://doi.org/10.1109/TVT.2019.2950538.

[5] Mylonopoulos F, Polinder H, Coraddu A. A comprehensive review of modeling and optimization methods for ship energy systems. IEEE Access 2023;11:32697–707. https://doi.org/10.1109/ACCESS.2023.3263719.

[6] Bassam AM, Phillips AB, Turnock SR, Wilson PA. Sizing optimization of a fuel cell/battery hybrid system for a domestic ferry using a whole ship system simulator. In: International Conference on Electrical Systems for Aircraft, Railway, Ship Propulsion and Road Vehicles and International Transportation Electrification Conference (ESARS-ITEC); 2016 Nov 2–4; Toulouse, France. Doi: 10.1109/ESARS-ITEC.2016.7841333.

[7] Pivetta D, Dall'Armi C, Taccani R. Multi-objective optimization of hybrid PEMFC/Li-ion battery propulsion systems for small and medium-size ferries. Int J Hydrogen Energy 2021;46(72):35949–60. https://doi.org/10.1016/j.ijhydene.2021.02.124.

[8] Dall'Armi C, Pivetta D, Taccani R. Health-conscious optimization of long-term operation for hybrid PEMFC ship propulsion systems. Energies3813 2021;14(13). https://doi.org/10.3390/en14133813.

[9] Dall'Armi C, Pivetta D, Taccani R. Uncertainty analysis of the optimal health-conscious operation of a hybrid PEMFC coastal ferry. Int J Hydrogen Energy 2022;47(21):11428–40. https://doi.org/10.1016/j.ijhydene.2021.10.271.

[10] Sun Y, Xu Q, Yuan Y, Yang B. Optimal energy management of fuel cell hybrid electric ships considering fuel cell aging cost. In: 2020 IEEE IAS Industrial and Commercial Power Systems Asia (I&CPS Asia); 2020 Jul 13–15; Weihai, China. 2020. Doi: 10.1109/ICPSAsia48933.2020.9208534.

[11] Zhang Z, Guan C, Liu Z. Real-time optimization energy management strategy for fuel cell hybrid ships considering power sources degradation. IEEE Access 2020;8:87046–59. https://doi.org/10.1109/ACCESS.2020.2991519.

[12] Han J, Charpentier JF, Tang T. An energy management system of a fuel cell/battery hybrid boat. Energies 2014;7(5):2799–820. https://doi.org/10.3390/en7052799.

[13] Bassam AM, Phillips AB, Turnock SR, Wilson PA. Development of a multi-scheme energy management strategy for a hybrid fuel cell driven passenger ship. Int J Hydrogen Energy 2017;42(1):623–35. https://doi.org/10.1016/j.ijhydene.2016.08.209.

[14] Bassam AM, Phillips AB, Turnock SR, Wilson PA. An improved energy management strategy for a hybrid fuel cell/battery passenger vessel. Int J Hydrogen Energy 2016;41(47):22453–64. https://doi.org/10.1016/j.ijhydene.2016.08.049.

[15] Zhao ZH. Improved fuzzy logic control-based energy management strategy for hybrid power system of FC/PV/battery/SC on tourist ship. Int J Hydrogen Energy 2022;47(16):9719–34. https://doi.org/10.1016/j.ijhydene.2022.01.040.

[16] Zhu L, Han J, Peng D, Wang T, Tang T, Charpentier JF. Fuzzy logic-based energy management strategy for a fuel cell/battery/ultracapacitor hybrid ship. In: 1st International Conference on Green Energy (ICGE 2014); 2014 Mar 25–27; Sfax, Tunisia. Doi: 10.1109/ICGE.2014.6835406.

[17] Fan F, Aditya V, Xu Y, Cheong B, Gupta AK. Robustly coordinated operation of a ship microgrid with hybrid propulsion systems and hydrogen fuel cells. Appl Energy 2022;312:118738. https://doi.org/10.1016/j.apenergy.2022.118738.

[18] Vieira GTT, Pereira DF, Taheri SI, Khan KS, Salles MBC, Guerrero JM, et al. Optimized configuration of diesel engine–fuel cell–battery hybrid power systems in a platform supply vessel to reduce CO_2 emissions. Energies 2022;15(6):2184. https://doi.org/10.3390/en15062184.

[19] Wang X, Shipurkar U, Haseltalab A, Polinder H, Claeys F, Negenborn RR. Sizing and control of a hybrid ship propulsion system using multi-objective double-layer optimization. IEEE Access 2021;9:72587–601. https://doi.org/10.1109/ACCESS.2021.3080195.

[20] Wu P, Bucknall R. Hybrid fuel cell and battery propulsion system modelling and multi-objective optimisation for a coastal ferry. Int J Hydrogen Energy 2020;45(4):3193–208. https://doi.org/10.1016/j.ijhydene.2019.11.152.

[21] Si Y, Wang R, Zhang S, Zhou W, Lin A, Zeng G. Configuration optimization and energy management of hybrid energy system for marine using quantum computing. Energy 2022;253:124131. https://doi.org/10.1016/j.energy.2022.124131.

[22] Chen H, Zhang Z, Guan C, Gao H. Optimization of sizing and frequency control in battery/supercapacitor hybrid energy storage system for fuel cell ship. Energy 2020;197:117285. https://doi.org/10.1016/j.energy.2020.117285.

[23] Ganjian M, Bagherian Farahabadi H, Alirezapouri MA, Rezaei FM. Optimal design strategy for fuel cell-based hybrid power system of all-electric ships. Int J Hydrogen Energy 2024;50:1558–71. https://doi.org/10.1016/j.ijhydene.2023.07.258.

[24] Mylonopoulos F, Kopka T, Coraddu A, Polinder H. A model-based parametric study for comparison of system configurations and control of a hydrogen hybrid cargo vessel. In: Modelling and Optimisation of Ship Energy Systems (MOSES 2023); 2023 Oct 26–27; Delft, Netherlands. Doi: 10.59490/moses.2023.671.

[25] Mylonopoulos F, Durgaprasad S, Coraddu A, Polinder H. Lifetime design, operation, and cost analysis for the energy system of a retrofitted cargo vessel with fuel cells and batteries. Int J Hydrogen Energy 2024;91:1262–73. https://doi.org/10.1016/j.ijhydene.2024.10.235.

[26] Marine – PowerCell Group: hydrogen fuel cell solutions [Internet]. PowerCell Sweden AB; [cited 2023 Jun 21]. Available from: https://powercellgroup.com/segments/marine/.

[27] Banaei M, Ghanami F, Khooban MH, Boudjadar J. Cost-effective control of roll-on/roll-off emission-free ships. In: 25th International Conference on Methods and Models in Automation and Robotics (MMAR 2021); 2021 Aug 23–26; Międzyzdroje, Poland. Doi: 10.1109/MMAR49549.2021.9528473.

[28] Ehret U, Neuper M. Applying the ramer-douglas-peucker algorithm to compress and characterize time-series and spatial fields of precipitation. EGU2014 -13537 Available from: Geophys Res Abstr 2014;16. https://meetingorganizer.copernicus.org/EGU2014/EGU2014-13537.pdf.

[29] GreenBattery – Praxis Automation Technology B.V. [Internet]. Praxis Automation Technology B.V.; [cited 2024 Mar 1]. Available from: https://www.praxis-automation.eu/products/electricenergy-storage/.

[30] Bureau Veritas. Bureau Veritas unveils rules for hydrogen-fuelled ships [Internet]. [cited 2025 Feb 10]. Available from: https://marine-offshore.bureauveritas.com/newsroom/bureau-veritas-unveils-rules-hydrogen-fuelled-ships.

[31] DNV. Handbook for hydrogen fuelled vessels: MarHySafe JDP Phase 1 [Internet]. Hovik, Norway: DNV; 2021 [cited 2025 Feb 13]. Available from: https://www.dnv.com/maritime/publications/handbook-for-hydrogen-fuelled-vessels-download/.

[32] Pratt JW, Klebanoff LE. Optimization of zero emission hydrogen fuel cell ferry design, with comparisons to the SF-BREEZE. Livermore (CA): Sandia National Laboratories; 2018 Jan. Report No.: SAND2018-0421. 190 p. Available from: https://rosap.ntl.bts.gov/view/dot/43799.

[33] Drube TK, Gerlach JM, Leach TS, Vogel B, Klebanoff LE. Exploring variations in the weight, size and shape of liquid hydrogen tanks for zero-emission fuel-cell vessels. Int J Hydrogen Energy 2024;80:1441–65. https://doi.org/10.1016/j.ijhydene.2024.06.420.

[34] Pratt JW, Klebanoff LE. Feasibility of the SF-BREEZE: a zero-emission, hydrogen fuel cell, high-speed passenger ferry. Livermore (CA): Sandia National

Laboratories; 2016 Sept. Report No. SAND2016-9719. 340 p. Available from: https://rosap.ntl.bts.gov/view/dot/51783.
[35] Klebanoff LE, Drube TK, Gerlach JM, Leach TS. Exploring liquid hydrogen tank technology for zero-emission fuel cell vessels. Livermore (CA): Sandia National Laboratories; 2024 Feb. Report No.: SAND2024-01678. 100 p. Available from: https://www.maritime.dot.gov/innovation/meta/exploring-liquid-hydrogen-tank-technology-zero-emission-fuel-cell-vessels.
[36] Yeh ST. Using trapezoidal rule for the area under a curve calculation. In: Proceedings of the 27th Annual SAS Users Group International Conference (SUGI 27); 2002 Apr 14–17; Orlando, FL. Paper 229-27. p. 1–5. Available from: https://support.sas.com/resources/papers/proceedings/proceedings/sugi27/p229-27.pdf.
[37] Aarskog FG, Danebergs J, Strømgren T, Ulleberg Ø. Energy and cost analysis of a hydrogen driven high speed passenger ferry. Int Shipbuild Prog 2020;67(1). https://doi.org/10.3233/ISP-190273.
[38] Kawasaki Heavy Industries Ltd. Kawasaki proves excellent thermal-insulation performance for liquefied hydrogen storage tanks [Internet]. 2023 Dec 11 [cited 2025 Feb 13]. Available from: https://global.kawasaki.com/en/corp/newsroom/news/detail/?f=20231211_8742.
[39] Fletcher T, Thring R, Watkinson M. An energy management strategy to concurrently optimise fuel consumption and PEM fuel cell lifetime in a hybrid vehicle. Int J Hydrogen Energy 2016;41(46):21503–15. https://doi.org/10.1016/j.ijhydene.2016.08.157.
[40] Metrohm. Fuel cells part 1 – what is a fuel cell? [Internet]. [cited 2025 Feb 13]. Available from: https://www.metrohm.com/en_nl/applications/application-notes/autolab-applikationen-anautolab/an-fc-001.html.
[41] Bestuzheva K, Chmiela A, Müller B, Serrano F, Vigerske S, Wegscheider F. Global optimization of mixed-integer nonlinear programs with SCIP 8. J Glob Optim 2023;91:287–310. https://doi.org/10.1007/s10898-023-01345-1.
[42] ABB. Traction inverters [Internet]. [cited 2025 Feb 13]. Available from: https://new.abb.com/electric-drivetrains/traction-inverters.
[43] Bye HM. Investigation of a 200 kW SiC-based IBC for high-speed hydrogen ferries [master's thesis]. Trondheim (Norway): Norwegian University of Science and Technology (NTNU); 2019. Available from: https://ntnuopen.ntnu.no/ntnu-xmlui/handle/11250/2625864?locale-attribute=no.
[44] ABB. Onboard DC Grid™ marine and ports – electric solutions [Internet]. [cited 2025 Feb 13]. Available from: https://new.abb.com/marine/systems-and-solutions/power-generation-and-distribution/onboard-dc-grid.
[45] ABB. Technical catalog: high voltage induction motors [Internet]. [cited 2025 Feb 13]. Available from: https://search.abb.com/library/Download.aspx?DocumentID=9AKK103508&LanguageCode=en&DocumentPartId=&Action=Launch=.
[46] ABB. ACS880 drive modules [Internet]. [cited 2025 Feb 13]. Available from: https://www.abb.com/global/en/product/drives/low-voltage-ac-drives/industrial-drives/acs880-drive-modules.
[47] Hitachi Nico Transmission Co. Marine gear capacity tables [Internet]. 2004 [cited 2025 Feb 13]. Available from: https://www.hitachi-nico.jp/nico_image/catalog/pdf/h_02.pdf.
[48] Shi W, Stapersma D, Grimmelius HT. Analysis of energy conversion in ship propulsion system in off-design operation conditions. WIT Trans Ecol Environ. 2009;121:1–12. Available from: https://www.witpress.com/Secure/elibrary/papers/ESUS09/ESUS09041FU1.pdf.
[49] Brouzas S, Zadeh M, Lagemann B. Essentials of hydrogen storage and power systems for green shipping. Int J Hydrogen Energy 2025;100:1543–60. https://doi.org/10.1016/J.IJHYDENE.2024.12.253.